# Chiral Resonant Modes Induced by Intrinsic Birefringence in Lithium Niobate Metasurfaces

Bo Wang[1,*] Tingyue Zhu,[2] Yunan Liu,[1] Haifang Yang,[1] Ruhao Pan[1,†] and Junjie Li[1,3,‡]

[1]*Beijing National Laboratory for Condensed Matter Physics, Institute of Physics, Chinese Academy of Sciences, 100190 Beijing, China*
[2]*School of Physical Science and Technology, Lanzhou University, 730000 Lanzhou, China*
[3]*CAS Key Laboratory of Vacuum Physics, University of Chinese Academy of Sciences, Beijing 100049, China*

The intrinsic chirality of natural materials is known to be weak, prompting extensive efforts to enhance chiral light-matter interactions on the metasurface platform. Chiral metasurfaces are typically created by manipulating the geometry of nanostructures, such as three-dimensional helical structures and slanted structures. However, these approaches are generally challenging to implement experimentally in optical frequency ranges. Here, we present the achievement of significant chirality on planar lithium niobate metasurfaces. We theoretically demonstrate that the birefringence of lithium niobate enables a strong coupling between two nearly degenerate resonant modes when rotating the optical axis. Despite the achiral geometric morphology of the lithium niobate structure, we show that these mixed modes exhibit chirality and can produce nearly full circular dichroism signals. Moreover, we experimentally validate our theoretical proposal using our advanced process technique for lithium niobate nanostructures and the measured circular dichroism signal reaches $-0.53$. These findings offer new possibilities for chiral metaphotonics.

Anisotropic material, such as crystals with noncubic lattices, plastics under mechanical stress, and liquid crystals, exhibit birefringence, where the refractive index depends on both the polarization and the direction of light propagation [1]. The birefringence in transparent natural media is typically small. Hence, many traditional optical devices that rely on birefringence, such as wave plates, Wollaston prisms, and polarizing cube beam splitters, are bulky, because the phase delay needs to be accumulated as the thickness increases. Instead, metasurfaces, artificially engineered surfaces that allow precise control and manipulation of electromagnetic waves [2–7], usually have a subwavelength thickness. Considerable effective birefringence [8] or shape birefringence [9] has been achieved on such thin metasurfaces by introducing anisotropic shapes to the structural elements. However, material birefringence, an intrinsic property of certain materials, has rarely been a focal point in the design and fabrication of metasurfaces. So far, metasurfaces have been typically made of isotropic materials, such as noble metals, high-index dielectrics like $TiO_2$, and amorphous silicon. Recent technological advancements have enabled the fabrication of metasurfaces using birefringent crystalline materials, such as crystalline lithium niobate (LN) films on insulating substrates [10–14].

However, large second-order nonlinear susceptibility $\chi^{(2)}$ is the starting point for metasurfaces on the LN platform, instead of the birefringence of LN.

One of the remarkable capabilities of metasurfaces is to increase chiral-optical response by creating chiral resonant modes on metasurfaces [15–17], which can exhibit near-unity circular dichroism (CD) signals under normally incident light. These chiral metasurfaces have application prospects in biosensing [18], quantum optics [19], and photochemistry [20]. Chiral resonant modes on metasurfaces usually result from geometric chirality of the building structures, such as subwavelength helices [21,22], some simpler asymmetric shapes with mirror symmetry broken [15,16], or asymmetric lattice [23]. Recent research has also shown that the extremely weak chirality of natural chiral enantiomers can induce strong coupling between two bound states in the continuum (BICs) on achiral metasurfaces [24], resulting in chiral BICs with CD signals that are 3 orders of magnitude higher than those without strong coupling. While the birefringence of transparent crystals is weak, it is typically stronger than the chirality of natural chiral enantiomers. It remains an open question whether birefringence can induce strong coupling between two resonances of metasurfaces.

Here, we theoretically and experimentally show that the birefringence of crystallized LN materials can induce strong coupling between two resonant modes supported by planar metasurfaces. Unlike other planar metasurfaces

---

*Contact author: wangbo2014@iphy.ac.cn
†Contact author: panruhao@iphy.ac.cn
‡Contact author: jjli@iphy.ac.cn
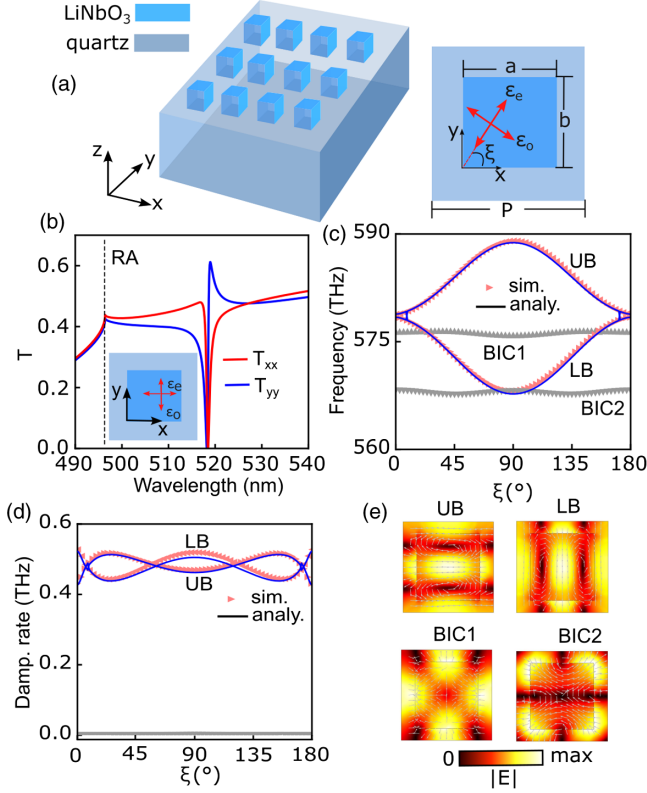
FIG. 1.   (a) Schematic of LN metasurface structure. (b) Simulated transmission spectra of $x$-polarization and $y$-polarization light incidence when $\xi = 0°$. (c),(d) Resonant frequencies and damping rates varying with $\xi$. The lines (triangle markers) denote analytical (simulated) results. (e) Simulated electric field profiles.

on a semi-infinite substrate which only can exhibit tiny intrinsic chirality [25,26], we show that the mixed resonant states can exhibit giant chirality which generates considerable CD signals. Our findings provide a new design degree of freedom to amplify chiroptical effects on the metasurface platform.

We first show the concept of material birefringence-induced coupling between two resonant modes. Figure 1(a) shows the structure of the LN metasurface. It is composed of periodic LN nanocubes, which are arranged in a square lattice with period $p = 340$ nm on a fused quartz substrate ($n_s = 1.46$). The thickness of LN films is 300 nm. Crystalline LN has negative uniaxial birefringence with $n_o - n_e \approx 0.06$ in the visible spectral range [27] ($n_e$ and $n_o$ denote extraordinary and ordinary refractive indices, respectively). This metasurface structure has $C_{2v}$ point symmetry with $\sigma_{xz}$, $\sigma_{yz}$ mirror symmetry and $C_2$ rotation symmetry if the birefringence of LN is neglected. In-plane mirror symmetry $\sigma_{xy}$ is broken due to the presence of a substrate. Taking account into the birefringence, both $\sigma_{xz}$ and $\sigma_{yz}$ can be broken when the extraordinary axis of LN deviates from the $x$ axis and the $y$ axis ($\xi \neq 0°$ and $\xi \neq 90°$, $\xi$ is the angle between the $x$ axis and the extraordinary axis), see Fig. 1(a). In this case, optical resonant modes at the $\Gamma$

point of the Brillouin zone (BZ) associated with different irreducible representations of $C_{2v}$ group can be coupled and chiral resonant sates emerge.

We use perturbation theory to solve the resonant frequencies of the LN metasurfaces when $\xi \neq 0°$. The LN metasurface with $\xi = 0°$ is then regarded as the unperturbed system, which is governed by the Maxwell equations:

$$\nabla \times \mathbf{E}_n = -i\omega_n \mu_0 \mathbf{H}_n,$$
$$\nabla \times \mathbf{H}_n = i\omega_n \epsilon_0 \boldsymbol{\varepsilon}_0 \mathbf{E}_n. \tag{1}$$

Here, subscripts ($n = 1, 2$ label the two resonances and $\boldsymbol{\varepsilon}_0$ is a diagonal matrix in the coordinate frame $(xoy)$ defined in Fig. 1(a), $\boldsymbol{\varepsilon}_0 = \mathrm{diag}(\varepsilon_e, \varepsilon_o)$, where $\varepsilon_o$ ($\varepsilon_e$) is the dielectric function along the ordinary (extraordinary) axis of the LN crystal, and $\epsilon_0$ and $\mu_0$ are permittivity and permeability of free space. When $\xi \neq 0°$, the dielectric tensor in the same coordinate system is not diagonal and possesses an increment:

$$\delta\boldsymbol{\varepsilon} = (\varepsilon_o - \varepsilon_e) \begin{bmatrix} \sin^2\xi & -\sin(2\xi)/2 \\ -\sin(2\xi)/2 & -\sin^2\xi \end{bmatrix}. \tag{2}$$

It is the increment in Eq. (2) that causes the coupling between the two resonances in Eq. (1). The resonant frequencies of the mixed modes are governed by an effective Hamiltonian,

$$\mathcal{H} = \begin{bmatrix} p_1 + \kappa_1 \sin^2\xi & \kappa \sin(2\xi)/2 \\ \kappa \sin(2\xi)/2 & p_2 + \kappa_2 \sin^2\xi \end{bmatrix}^{-1} \begin{bmatrix} \omega_1 p_1 & 0 \\ 0 & \omega_2 p_2 \end{bmatrix} \tag{3}$$

where $p_n = \int_{uc} (\mathbf{E}_n \cdot \boldsymbol{\varepsilon}_0 \mathbf{E}_n - \mathbf{H}_n \cdot \mathbf{H}_n)dV$, $\kappa_n = (\varepsilon_o - \varepsilon_e) \int_{LN} (E_{nx}E_{nx} - E_{ny}E_{ny})dV$, $\kappa = (\varepsilon_e - \varepsilon_o) \int_{LN} (E_{1x}E_{2y} + E_{1y}E_{2x})dV$. The detailed derivations can be found in the Supplemental Material [28]. The two resonant frequencies ($\omega_U$ for upper energy level and $\omega_L$ for lower energy level) and the corresponding eigenstates ($a_U = [a_{Ux} \; a_{Uy}]^T$, $a_L = [a_{Lx} \; a_{Ly}]^T$) can be obtained by diagonalizing $\mathcal{H}$. Now, we have written closed-form expressions to analytically calculate the birefringence induced mode coupling between two resonant modes. The off-diagonal term $\kappa \sin(2\xi)/2$ mainly determines the couple strength [24]. We will show below that the CD signal from birefringence-induced mode coupling can reach nearly 1.

To achieve strong coupling strength, parameter $\kappa$ should be maximized as much as possible. It requires the non-perturbed resonances (resonances when $\xi = 0°$) to have large $Q$ factors and birefringence material to occupy large volume. Besides, the mode coupling must obey selection rules determined by the $C_{2v}$ point group, which has four one-dimension irreducible representations: $A_1$, $A_2$, $B_1$, and $B_2$. We show in the Supplemental Material [28] that the two
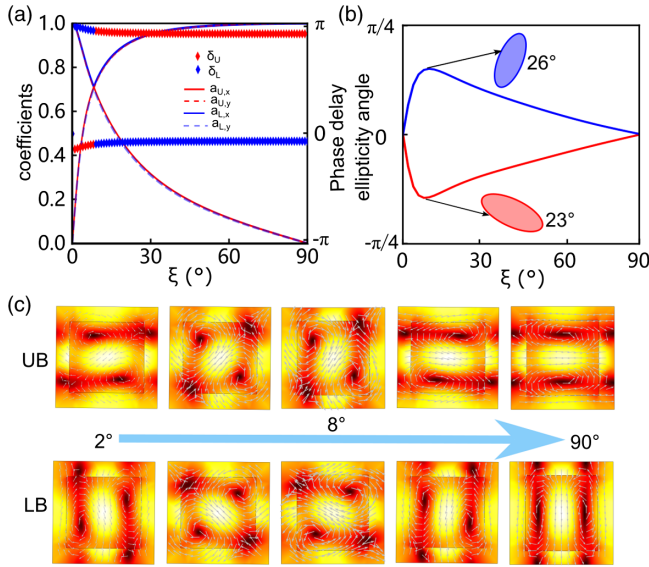
FIG. 2. (a) Calculated coefficients of the eigenvector of the effective Hamiltonian. Subscripts $U$ and $L$ labels upper and lower band while $x$ and $y$ labels the basis the effective Hamiltonian. (b) Ellipticity angle of the polarization ellipses of the far-field radiation for the LB and UB resonances. Insets: polarization ellipses at $\xi = 8°$. (c) Evolution of electric field profiles for the two bands with $\xi$.

nonperturbed resonances associated with $B_1$ (odd parity, even parity, and odd parity for $C_2$, $\sigma_{xz}$, and $\sigma_{yz}$ operations, respectively) and $B_2$ (odd parity, odd parity, and even parity for $C_2$, $\sigma_{xz}$, and $\sigma_{yz}$ operations, respectively) irreducible representations of $C_{2v}$ group can have nonzero coupling strength while other combinations are forbidden.

We then numerically study the structure shown in Fig. 1(a) using COMSOL MULTI PHYSICS software and Rigorous Coupled Wave Analysis (RCWA) solver [29] to validate our theory. In the COMSOL model, we set $\varepsilon_e$ and $\varepsilon_o$ of LN material as 5.06 and 5.46, respectively. The dispersions [27] of $\varepsilon_e$ and $\varepsilon_o$ are considered in RCWA. The structure parameters $a$ and $b$ are set as 250 and 237 nm, which results in a filling factor of nearly 51%. A large filling factor helps to increase the birefringence region, which contributes to enhancing birefringence-induced mode-coupling strength. We first simulated the transmission of normally incident lights with $x$ polarization and $y$ polarization by the uncoupled system ($\xi = 0°$). As shown in Fig. 1(b), the transmittance spectra $T_{xx}$ and $T_{yy}$ have nearly degenerate resonant dips at 518 nm, very close to the Rayleigh anomaly (RA) at 496 nm. To analyze these two resonances (UB for the upper band and LB for the lower band), we used the eigenfrequency solver to calculate the resonant frequencies, damping rates, and the corresponding electric-filed profiles at the $\Gamma$ point of the Brillouin zone, as shown in Figs. 1(c)–1(e). One can see in Fig. 1(e) that the electric field profile of the UB (LB) is transformed with $B_1$ ($B_2$) irreducible representation of the $C_{2v}$ group, which is

expected to have a nonzero coupling strength. Besides, there are two bound states in the continuum (BIC1 and BIC2) around the UB and LB with zero damping rates. Their electric field profiles [see Fig. 1(e)] are transformed with $A_1$ and $A_2$ irreducible representations of $C_{2v}$ group, respectively. As $\xi$ increases, the resonant frequencies of the UB and LB split dramatically while those of BIC1 and BIC2 remain nearly unchanged [see Figs. 1(c) and 1(d)], which is perfectly consistent with the selection rules that only resonances with $B_1$ and $B_2$ irreducible representations can be coupled when $\xi \neq 0°$. To validate the effective Hamiltonian in Eq. (3), we calculate the parameters $p_1$, $p_2$, $\kappa_1$, $\kappa_2$, and $\kappa$ with the simulated field profiles $\mathbf{E}_1$ and $\mathbf{E}_2$, and then substitute them into Eq. (3) to calculate resonant frequencies and damping rates. As shown in Figs. 1(c) and 1(d), the analytical results are in good agreement with the simulated ones.

The mode coupling not only introduces resonant frequency splitting, but also changes the polarization states of far-field radiations from linear polarization to elliptical polarization. When $\xi = 0°$, the UB resonance radiates the $x$-polarized light while LB resonance radiates the $y$-polarized light. As $\xi$ increases, the far-field radiations of the hybridized modes are the superposition of the original resonances, which can result in elliptical polarization. To gain further insight, we retrieve the coefficients of the hybridized modes projecting on the original resonances, that are the eigenvectors of the effective Hamiltonian. As shown in Fig. 2(a), $|a_{Uy}|$ and $|a_{Lx}|$ grow from zero as $\xi$ increases from zero. Meanwhile, the phase delay $\delta_U = \angle(a_{Uy}/a_{Ux})$ and $\delta_U = \angle(a_{Ly}/a_{Lx})$ start to deviate from zero and $\pi$. The electric field profiles, see Fig. 2(c), also change slightly compared with the original ones. When $\xi = 8°$, $a_{Ux} \approx a_{Uy} \approx a_{Lx} \approx a_{Ly}$, which means the coupling strength and the superposition is maximized. When $\xi > 8°$, $|a_{Uy}|$ and $|a_{Lx}|$ trend to become 0 and the field profiles gradually return to their original states. The ellipticity angle of the LB and the UB resonances are simulated and shown in Fig. 2(b). As expected, the ellipticity angles of the UB and the LB reach maximized (26° for the LB and 23° for the UB) at $\xi = 8°$ and have opposite signs, indicating opposite chirality of their far-field radiations.

The elliptically polarized far-field radiations of the resonant modes at the $\Gamma$ point of the BZ will give rise to a chiral optical response. To reveal the chiral optical response, we calculate the copolarization transmission of left circularly polarized (LCP) and right circularly polarized (RCP) incidences, shown in Figs. 3(a) and 3(b). The asymmetric transmission, $T_{RCP} - T_{LCP} \neq 0$, at both the UB and LB resonances are obviously observed as $\xi$ deviates from 0° and 90°. Figures 3(c) and 3(d) show the simulated circular dichroism spectra, which are defined as $CD = (T_{RCP} - T_{LCP})/(T_{RCP} + T_{LCP})$, which exhibits remarkable CD signal for both LB and UB resonances. At $\xi = 8°$, the CD signal for UB is $-0.96$. At a single $\xi$, CD for
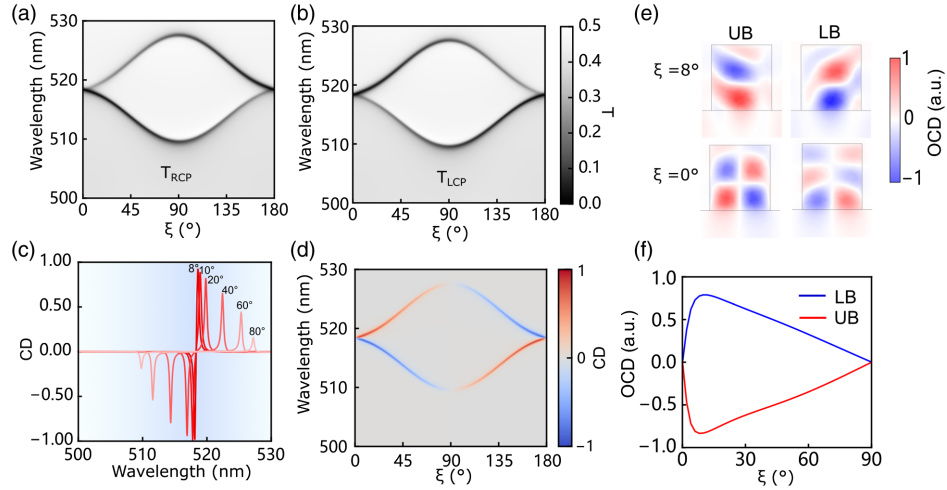
FIG. 3. (a),(b) Simulated copolarization transmission spectra $T_{\mathrm{RCP}}$ for RCP (a) and $T_{\mathrm{LCP}}$ for LCP (b) incidences. (c) Selected CD spectra at different $\xi$. (d) Simulated CD spectra with a continuously varying $\xi$. (e) Cross-sectional optical chiral density distributions when $\xi = 0°$ and $\xi = 8°$. (f) Integrated optical chirality density (OCD) over the whole unit cell as a function of $\xi$.

LB and UB resonances have an opposite sign, which is consistent with analytic results in Fig. 2(a) that $\delta_L$ and $\delta_U$ have a phase difference of nearly $\pi$ and that the far-field radiations of the LB and UB resonances have an opposite chirality. In the same band, CD signals at $\xi$ and $\pi - \xi$ have the same values and opposite signs. This can be explained by the sign transition of the coupling term $\kappa \sin(2\xi)$ in the $\mathcal{H}$. The origin of the chiral optical response can also be revealed by the optical chirality density: $\mathrm{OCD} = -1/2\omega\mathrm{Re}[\mathbf{D} \cdot \mathbf{B}^*]$, where $\mathbf{B}, \mathbf{D}, \omega$ are magnetic flux density, the electric displacement field, and angular frequency of light, respectively. Nonzero OCD integrated over the whole unit cell, $\int_{uc} \mathrm{OCD}dV$, will generate optical chirality flux, which produces a chiral optical response. When $\xi = 0°$, the mirror symmetry $\sigma_{xz}$ and $\sigma_{yz}$ is preserved. The OCD distributions have odd parity, as shown in Fig. 3(e), and thus $\int_{uc} \mathrm{OCD}dV = 0$ even though the in-plane mirror symmetry $\sigma_{xy}$ is breaking. When $\xi \neq 0°$ and $\xi \neq 90°$, the OCD distributions are asymmetric [see Fig. 3(e)], the OCD integration has nonvanished values, as shown in Fig. 3(f), and has opposite values for LB and UB resonances. Consistent with previous analysis, the OCD integration reaches a maximized value at $\xi = 8°$.

For the experiment demonstration, we fabricated the proposed metasurfaces on a commercial available LN films with the thickness of 300 nm on quartz substrate. The LN films were patterned with electron beam lithography and etched with inductively coupled plasma reactive ion etching technique. The etching gases and their ratio of ICP-RIE were carefully chosen to realize high fill-ratio LN nanostructures. The detailed etching technique can be found in our previous paper [30]. The scanning electron microscope images of the fabricated LN metasurfaces are shown in Fig. 4(a). The variation of $\xi$ was realized by rotating the whole metasurfaces against the $e$ axis of the LN film, as

shown in the insets of Figs. 4(b) and 4(d). This is different from the previous report where the structure was rotated in the unit cells [31]. In our case, if neglecting the birefringence, the cross-polarization transmission of circularly polarized light only obtains a geometric phase and the absolute value of transmittance is not changed when $\xi$ is changed. Our theoretical analysis above and experiments below demonstrate that, in the presence of birefringence, the frequencies and chirality of the resonant modes can be remarkably changed by varying $\xi$. The copolarization transmission spectra under the illumination of circularly polarized lights are measured by a custom-built microscopy setup (see details in the Supplemental Material [28]). Figures 4(b) and 4(d) show the measured transmission
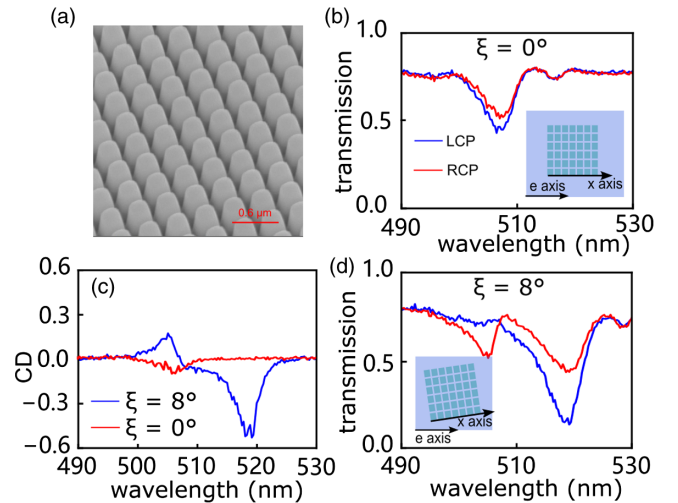


FIG. 4. (a) Scanning electron microscopy (SEM) images of the typical fabricated LN metasurfaces. (b),(d) Measured copolarization transmission spectra of circularly polarized light incidence at $\xi = 0°$ (b) and $\xi = 8°$(d). (c) Measured CD spectra.

spectra at $\xi = 0°$ and $\xi = 8°$, respectively. One can find that the resonant frequency splitting happens when $\xi$ changes from $0°$ to $8°$. We also observed obvious asymmetric transmission when $\xi = 8°$ while only a slight asymmetric transmission in the case of $\xi = 0°$. Figure 4(c) presents the measured CD spectra where the curve for $\xi = 0°$ is almost flat and presents only a tiny CD signal. In contrast, the CD spectra at $\xi = 8°$ present two obvious chiral resonances with opposite signs. At the resonant wavelength of 520 nm, the CD signal reaches $-0.53$. These experimental results validate the main features of our theoretical prediction of the chiral resonant modes induced by the birefringence. The discrepancies between experimental and simulated CD signals are attributed to dimensional deviations and slanting sidewalls in the real samples (see details in the Supplemental Material [28]). Other imperfections, such as the rough surfaces, are also non-negligible.

In conclusion, we have shown in theory and experiments that the birefringence of LN material can induce strong coupling between two resonant modes of the LN metasurface. The hybridized modes due to the strong coupling are elliptically polarized with opposite chirality and thus generate considerable CD signals. These results are incredible because both the material and spatial structure are achiral but their combination can exhibit giant chirality. Hence, our research paves a new way to control chiroptical effect. Furthermore, since the crystalline LN is an excellent candidate for second-order nonlinear optical process [32,33], our design can be used in nonlinear chiral metaphotonics [34].

*Data availability*—The data that support the findings of this Letter are openly available [36].

[1] M. Born and E. Wolf, *Principles of Optics: Electromagnetic Theory of Propagation, Interference and Diffraction of Light* (Elsevier, New York, 2013).

[2] H.-T. Chen, A. J. Taylor, and N. Yu, Rep. Prog. Phys. **79,** 076401 (2016).

[3] N. Yu and F. Capasso, Nat. Mater. **13,** 139 (2014).

[4] F. Ding, A. Pors, and S. I. Bozhevolnyi, Rep. Prog. Phys. **81,** 026401 (2017).

[5] A. I. Kuznetsov, M. L. Brongersma, J. Yao, M. K. Chen, U. Levy, D. P. Tsai, N. I. Zheludev, A. Faraon, A. Arbabi, N. Yu *et al.*, ACS Photonics **11,** 816 (2024).

[6] Q. Fan, M. Liu, C. Zhang, W. Zhu, Y. Wang, P. Lin, F. Yan, L. Chen, H. J. Lezec, Y. Lu, A. Agrawal, and T. Xu, Phys. Rev. Lett. **125,** 267402 (2020).

[7] P. Genevet, F. Capasso, F. Aieta, M. Khorasaninejad, and R. Devlin, Optica **4,** 139 (2017).

[8] D. Keene, M. LePain, and M. Durach, Ann. Phys. (Berlin) **528,** 767 (2016).

[9] Z. Shi, A. Y. Zhu, Z. Li, Y.-W. Huang, W. T. Chen, C.-W. Qiu, and F. Capasso, Sci. Adv. **6,** eaba3367 (2020).

[10] B. Gao, M. Ren, W. Wu, H. Hu, W. Cai, and J. Xu, Laser Photonics Rev. **13,** 1800312 (2019).

[11] L. Carletti, C. Li, J. Sautter, I. Staude, C. De Angelis, T. Li, and D. N. Neshev, Opt. Express **27,** 33391 (2019).

[12] J. Zhang, J. Ma, M. Parry, M. Cai, R. Camacho-Morales, L. Xu, D. N. Neshev, and A. A. Sukhorukov, Sci. Adv. **8,** eabq4240 (2022).

[13] A. Fedotova, L. Carletti, A. Zilli, F. Setzpfandt, I. Staude, A. Toma, M. Finazzi, C. De Angelis, T. Pertsch, D. N. Neshev *et al.*, ACS Photonics **9,** 3745 (2022).

[14] L. Hu, B. Wang, Y. Guo, S. Du, J. Chen, J. Li, C. Gu, and L. Wang, Adv. Opt. Mater. **10,** 2200193 (2022).

[15] M. V. Gorkunov, A. A. Antonov, and Y. S. Kivshar, Phys. Rev. Lett. **125,** 093903 (2020).

[16] A. Overvig, N. Yu, and A. Alù, Phys. Rev. Lett. **126,** 073001 (2021).

[17] Y. Chen, H. Deng, X. Sha, W. Chen, R. Wang, Y.-H. Chen, D. Wu, J. Chu, Y. S. Kivshar, S. Xiao, and C.-W. Qiu, Nature (London) **613,** 474 (2023).

[18] O. Ávalos-Ovando, E. Y. Santiago, A. Movsesyan, X.-T. Kong, P. Yu, L. V. Besteiro, L. K. Khorashad, H. Okamoto, J. M. Slocik, M. A. Correa-Duarte, M. Comesaña-Hermo, T. Liedl, Z. Wang, G. Markovich, S. Burger, and A. O. Govorov, ACS Photonics **9,** 2219 (2022).

[19] P. Lodahl, S. Mahmoodian, S. Stobbe, A. Rauschenbeutel, P. Schneeweiss, J. Volz, H. Pichler, and P. Zoller, Nature (London) **541,** 473 (2017).

[20] C. He, G. Yang, Y. Kuai, S. Shan, L. Yang, J. Hu, D. Zhang, Q. Zhang, and G. Zou, Nat. Commun. **9,** 5117 (2018).

[21] M. Esposito, V. Tasco, F. Todisco, M. Cuscunà, A. Benedetti, M. Scuderi, G. Nicotra, and A. Passaseo, Nano Lett. **16,** 5823 (2016).

[22] J. Kaschke, M. Blome, S. Burger, and M. Wegener, Opt. Express **22,** 19936 (2014).

[23] I. Toftul, P. Tonkaev, K. Koshelev, F. Lai, Q. Song, M. Gorkunov, and Y. Kivshar, Phys. Rev. Lett. **133,** 216901 (2024).

[24] Y. Chen, W. Chen, X. Kong, D. Wu, J. Chu, and C.-W. Qiu, Phys. Rev. Lett. **128,** 146102 (2022).

[25] T. Shi, Z.-L. Deng, G. Geng, X. Zeng, Y. Zeng, G. Hu, A. Overvig, J. Li, C.-W. Qiu, A. Alù, Y. S. Kivshar, and X. Li, Nat. Commun. **13,** 4111 (2022).

[26] R. Zhao, T. Koschny, and C. M. Soukoulis, Opt. Express **18,** 14553 (2010).

[27] U. Schlarb and K. Betzler, Phys. Rev. B **48,** 15613 (1993).

[28] See Supplemental Material at http://link.aps.org/supplemental/10.1103/PhysRevLett.134.113802 for detailed derivation of the

effective Hamiltonian model and selection rules, experimental details and influences of fabrication imperfections.

[29] V. Liu and S. Fan, Comput. Phys. Commun. **183**, 2233 (2012).

[30] Y. Liu, B. Wang, L. Hu, C. Li, X. Ji, G. Geng, R. Pan, H. Yang, and J. Li, Adv. Mater. Technol. **9**, 2400318 (2024).

[31] D. Gryb, F. J. Wendisch, A. Aigner, T. G"olz, A. Tittl, L. de S. Menezes, and S. A. Maier, Nano Lett. **23**, 8891 (2023).

[32] J. Ma, F. Xie, W. Chen, J. Chen, W. Wu, W. Liu, Y. Chen, W. Cai, M. Ren, and J. Xu, Laser Photonics Rev. **15**, 2000521 (2021).

[33] C. Wang, Z. Li, M.-H. Kim, X. Xiong, X.-F. Ren, G.-C. Guo, N. Yu, and M. Lončar, Nat. Commun. **8**, 2098 (2017).

[34] K. Koshelev, P. Tonkaev, and Y. Kivshar, Adv. Opt. Photonics **5**, 064001 (2023).

[35] https://cstr.cn/31123.02.SECUF

[36] B. Wang (2025), 10.6084/m9.figshare.28189436.v2.